Investigating the relationship between mechanical properties and residual stress in the laser cladding process of Inconel 625 superalloy

Mohammad Reza Borhani [a], Mohammad Rajabi [a], Reza Shoja Razavi [b,*], Roohollah Jamaati [a]

[a] Department of Materials Engineering, Babol Noshirvani University of Technology, Babol, 47148-71167, Iran
[b] Faculty of Materials & Manufacturing Technologies, Malek Ashtar University of Technology, Iran

A B S T R A C T

In the present study, the tensile strength, fracture surface, hardness, and amount of residual stress in Inconel 625 super alloy cladded with direct metal deposition (DLD) process in the states before and after stress relief was studied. Residual stresses on the cladding layer surface were determined via XRD method. According to results, the yield strength of Am sample increased by 10% compared to thecast sample (reference sample). Although the yield strength experiebced an increase, the ductility followed an opposite trend falling from 42.5% to 26%. According to residual stress test outcomes, tensile residual stress of 361 MPa in the additive-manufactured sample. After stress relaxation heat treatment and almost complete removal of residual stress, the ductility reached 52.5%, the ultimate strength was also improved by 17% from cast sample. Also, after stress relaxation, the hardness of the sample and its fluctuations are reduced.

1. Introduction

In direct laser deposition, residual stress can be observed when deposited materials experience quick changes in temprature. Residual stress may cause a sharp decrease in the fracture resistance. Appropriate heat treatment can release stresses. However, the deformation created during the cladding process may lead to incompatibility with the desired geometry and even deteriorate the uniformity of the product or generally, the quality of the cladding [1–3].

Inconel 625 is its unique weldability and the stability of its crystal structure at high temperatures, which maintains the grain structure after remelting [4,5]. Direct laser deposition is considered a developing methods of manufacturing and renovating parts. In this method, metal powder is fed simultaneously with a high-energy laser beam, which causes rapid melting of the feeding powder and, consequently, additive manufacturing of the powder, as mentioned above, on a substrate. The solidified structure contributes greatly in determining mechanical properties of the produced part. Generally, laser cladding processes have high heating and cooling speeds, especially at the solid-melt interface, with values around 10^8 K/s. The lack of required time for the formation and growth of grains, leads to the creation of a fine-grained structure [2,3].

In the laser cladding process, due to the input heat, a high-temperature gradient is created. During the cooling, these gradients, coupled with different material properties, lead to different thermal contractions, and consequently, high residual stresses can be

---

found in the cladding layers [1–3]. When the tensile residual stresses in the deposited layers are high, the formation of cracks are almost guaranteed. Often, these cracks extend perpendicular to cladding direction, which indicates that the stresses are the highest along the cladding direction. Controling the cladding process directly impacts these aforementioned residual stresses [6].

The results of Rombus et al. [7] research showed a fine and dendritic structure formed by rapid solidification on additively manufactured IN625 superalloy. The dendrites in this microstructure included in the direction of construction. In addition, the mechanical properties have been investigated in the vertical and parallel directions. Results showed that the final strength in perpendicular to the structure is equal to 1000 MPa, While this strength in the direction parallel to the structure is equal to 882 MPa. Unlike strength, ductility is 36% in parallel mode and 24% in vertical way. The first factor mentioned for higher strength is the orientation of the dendrites. The next factor is the difference in heat flow in the direction of construction and perpendicular to it. In another study conducted by Dinda et al. [8], similar results were obtained. Furthermore, the properties of direct-laser-deposited materials are dependent on the direction, and according to the directional solidification, the properties change; therefore, it can be seen that the metal texture, which represents the orientation of the grains in the structure, can impact the final properties of the direct-laser-deposited sample.

Kermani et al. [9] investigated on the IN718 a.m. process; Considering that of the changes in the movement pattern in this article were effective on the microstructure, and ultimately, the amount of residual stress, the movement pattern affects the cooling speed and dendritic structure.

During laser cladding, the molten pool is formed. The powder is fed into the molten pool via a nozzle using an inert carrier. During plating, a surface is cladded by overlapping multiple plating paths (called plating layers). High cooling rates, nonlinear material properties at high temperatures, and differential shrinkage are characteristics of the laser cladding process [10–12].

According to Turnbull's theory, the energy barrier ΔG for the nucleation of crystal on the substrate is from the relation $\Delta G = \frac{4\pi\gamma_{LC}^3 T_m^2}{3(\Delta H_m \Delta T)^2}\left(2 - 3\cos\theta + \cos^3\theta\right)$. In this regard, the γ_{LC} parameters represent the surface energy of the melt interface, T_m demonstrates the equilibrium melting temperature, ΔH_m represents the melting latent heat, ΔT shows the amount under solidification below the temperature T_m, and θ represents the contact angle. In the event that it makes the surface more perfect, the contact angle θ becomes zero; Therefore, ΔG will also be zero. In this case, the crystal will germinate on the field without overcoming the energy barrier. If there is no background or if the melt cannot make the surface of the experience ultimately, the energy barrier will be very high [13]. According to investigations, the increment in the cooling rate which translates to reduction in the solidification time, leads to a finer (cellular or dendritic) structure. This relationship is $d = at_f^n = b(\varepsilon)^{-n}$, Where d is the distance between the arms of secondary dendrites, t_f is the local solidification time, ε is the cooling rate, a, n and b are proportional constants. The cooling rate increases when the solid-melt interface reaches the surface. The reduction in the rate of cooling while the solidification is undergoing, lets the dendrite have more time, and thus the distance between dendritic arms increases [14].

Fang et al. [15] investigated the mechanical properties of a direct-laser-deposited IN625 sample. Test results indicated that the final strength of the AM was 812 MPa, and its ductility was 13%. The structure of the alloy after deposition had irregular shape. It had a lava phase (containing refractory elements such as Nb and Mo) and carbide deposits in the inter-dendritic region. As a way of improving the properties and increasing the ductility, the sample underwent heat treatment at three temperatures of 1000, 1100, and 1200 °C for 1 h. When the temperature went up from 1000 °C to 1200 °C, the lave phase deposits dissolved, which will lead to a complete morphology change. The overall morphology changes from a relatively irregular shape to a food bar and block shape, which is a positive change regarding the improvement of the plastic toughness of the alloy. After the heat treatment, the γ-Ni solid solution dramatically reduces the orientation of the crystalline grains. The elastic modulus of all samples is 270 GPa. By annealing at temperatures of 1000, 1100, and 1200 °C, the final strength increases by 12, 5, and 5% and ductility by 116, 138, and 99%, respectively.

Pruk et al. [16] reduced the residual stress of the thin-walled 304 stainless steel sample by 30%, utilizing local preheating. Following a similar method for a chromium-molybdenum steel sample made by laser deposition, Shimol et al. [17] used stress relaxation, laser heat treatment (rescanning), and preheating of the substrate to effectively bring the residual stress down by 70, 55 and 40%, respectively. One of the other ways to minimize residual stress is by changing the scanning pattern. Denlinger et al. [18] reduced the residual stress of Ti6Al4V titanium alloy and Inconel 625 samples by 55% by changing the laser stopping time between layers. In their research, they reached the minimum residual stress by reducing the inter-pass pauses. It is worth noting that the Ti6Al4V samples have significantly different residual stresses compared to the Inconel 625 samples. It is mainly due to the higher heat transfer rates in Ti6Al4V alloy, and less heat accumulates in it.

Other articles commonly suggest that the reduction in the temperature gradient through substrate preheating or stress relaxation after complete fabrication makes the residual stress follow the same decreasing trend. However, these techniques are faced with limitations. Decreasing the temperature gradient through the reduction of the heat input, which is an important design parameter, will directly decrease the efficiency of manufacturing and therefore, it is a limiting factor. Today, the X-ray diffraction is a widely utilized method for calculating residual stress. This measurement method, which is a non-destructive and established technique, allows accurate and spatially resolved stress measurement in areas of several square millimeters without direct contact between the sample and the measuring probe. These features are suitable for stress evaluation in additive manufacturing processes such as direct laser deposition (DLD). The maximum residual stress happens a few millimeters before the melt, in which an extensometer aperture cannot be effectively placed [19–21]. The stress measurement by X-ray diffraction is not done directly, but strain must always be measured. The X-ray is counted at different angles, and then the residual stress is calculated by the $\sin^2\psi$ method and by using elasticity equations and relationships. The gradient of the line is obtained from several specific points in the $\theta = \sin^2\psi$ diagram using the least square method.

The genesis of this study's rationale is an extension of the principal challenge associated with residual stress formation and its
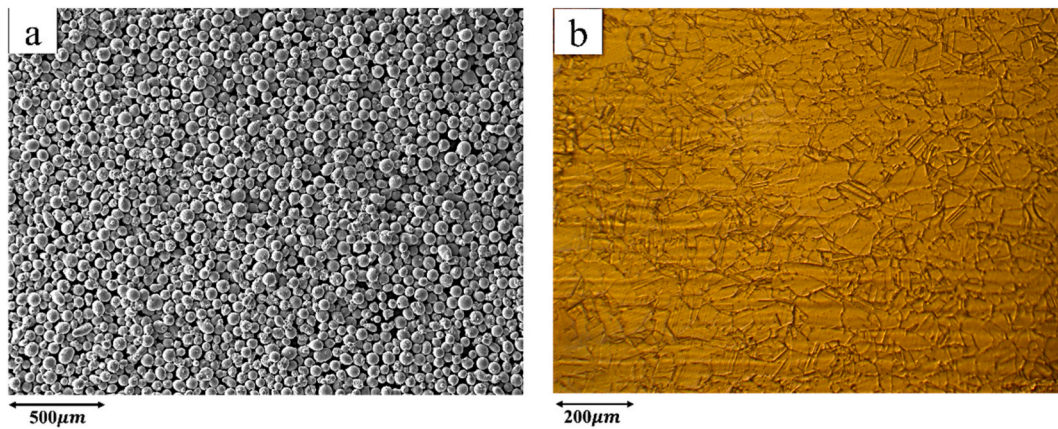
Fig. 1. Microscopic image of a)Inconel 625 powder, and b) substrate used in this research.

Table 1
Chemical composition of Inconel 625, including substrate and powder (wt%).

	Element	Ni	Fe	Cr	Nb	Mo	Ti	Al	Si	Mn	Other
Substrate	Content (Wt%)	Bal.	2	22.4	3.5	8.8	0.2	0.8	0.5	0.2	<0.2
Powder		Bal.	4	22.2	2.9	7.5	0.2	0.3	0.5	0.2	<0.2

subsequent relief in components formed through the (DLD) process, specifically for Inconel 625. This challenge takes precedence since unregulated residual stress within the substrate, accrued during processing, could potentially compromise the final characteristics of the component. This issue is of particular pertinence to components fabricated through additive manufacturing techniques. Consequently, this research is focused on the DLD process of Inconel 625, intending to offer insights that can optimize this process and improve the integrity of the produced parts.

To further this aim, our primary objective is to scrutinize and quantify the cooling rate of Inconel 625 during the DLD process. This was done using the secondary dendritic arm spacing (SDAS) as a benchmark, thus the correlation between the cooling rate and the genesis of residual stress was investigated. Subsequently, investigations were carried out on the accurately measure and evaluate the residual stress in samples processed via DLD process both prior to and following stress relief. This paves the way for a clearer understanding of the effectiveness of stress mitigation methods on reducing interior residual stress.

Next, another goal of this research is assess the impact of stress relief on the dendritic microstructure of the sample. This particular objective focuses on understanding the microstructural alterations that occur during the stress relief process. Thereafter, the assessment of hardness and tensile characteristics of samples before and after the stress relief gives an insight into how these mechanical properties fluctuate with the variation in process parameters.

Finally, the current study is aimed to compare the mechanical properties of the as-deposited Inconel 625 sample and a reference sample to elucidate whether the DLD-processed sample is comparable, superior or inferior to the reference sample concerning these basic properties. The successful accomplishment of these objectives not only has the potential to bridge the existing knowledge gap about the DLD process of Inconel 625 but also stands as a pivotal contributor to enhancing future additive manufacturing.

To achieve these objectives, a comprehensive experimental procedure was carried out including the following steps: Inconel 625 powder was deposited on a homogeneous substrate through DLD process. X-ray diffraction analysis validated that the substrate and the deposited cladding primarily consist of an FCC nickel-based austenitic phase (gamma phase). Then tensile tests were performed, the hardness was evaluated and finally the residual stress was calculated.

To examine the cooling rate during the DLD process, SDAS value was calculated at different locations on the sample. Stress relief heat treatment was conducted, followed by a re-evaluation of hardness and residual stress, enabling an understanding of the changes caused by stress relief.

2. Experimental

In this research, gas atomization IN625 powder with a particle size of 60–90 μm (Fig. 1(a)) was deposited by DLD process on a homogeneous substrate with austenitic microstructure (Fig. 1(b)). A DLD system was used to make the samples. The results of energy dispersive spectroscopy of powder and substrate are also shown in Table 1.

In preparing the substrate in the form of a tablet with a thickness of 5 mm, a grinding of up to 800 grit SiC paper was used to remove surface oxides (see Table 2). For sample printing, a laser power of 225 W,a scanning rate of 10 mm/s, and a powder feed rate of 150 mg/s with 45% transverse overlap and a unidirectional movement pattern were used [22,23].

Fig. 2(a) and 2(b) show the X-ray diffraction analysis of the substrate and the manufactured sample, respectively, in the
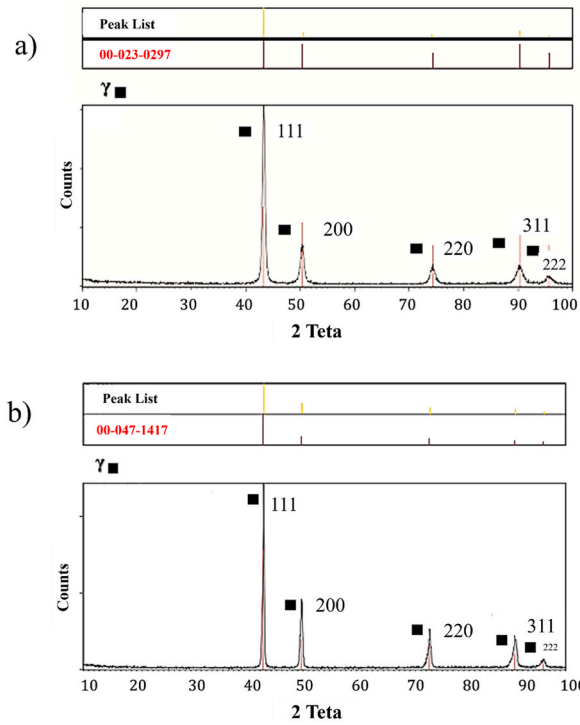
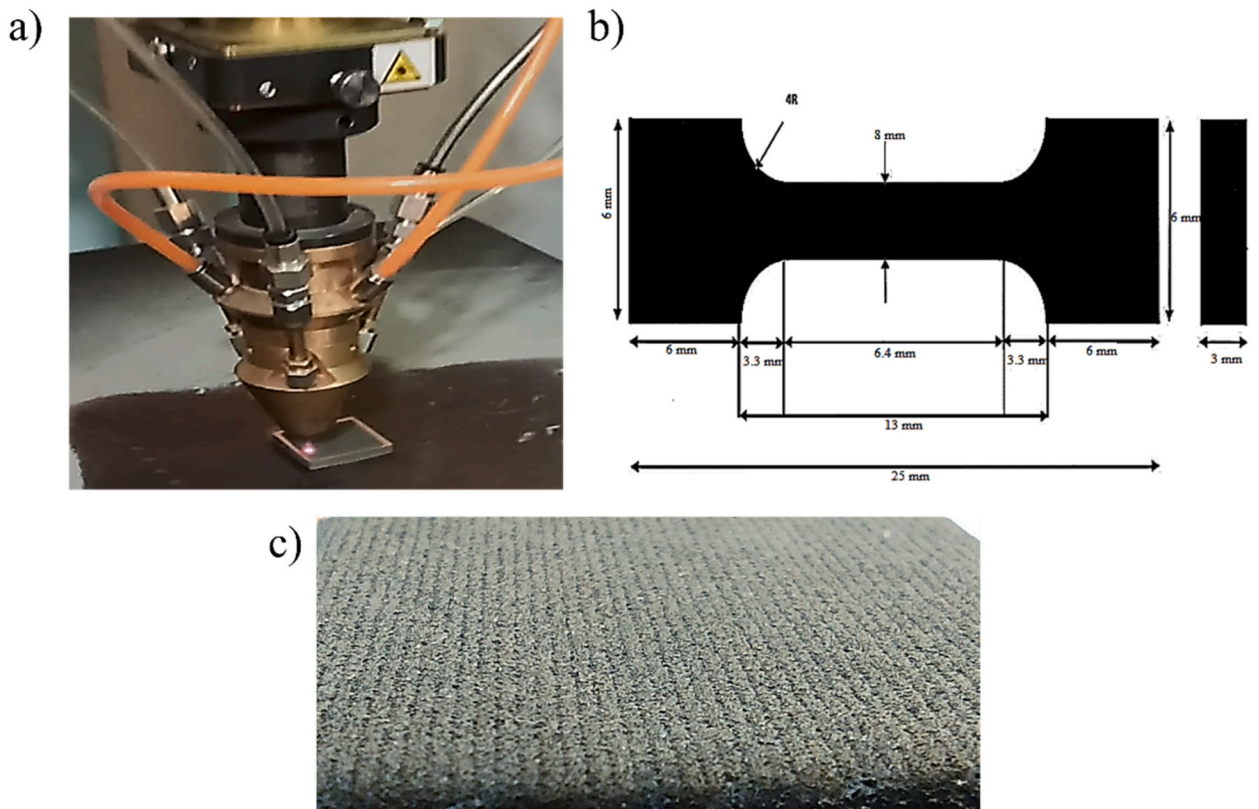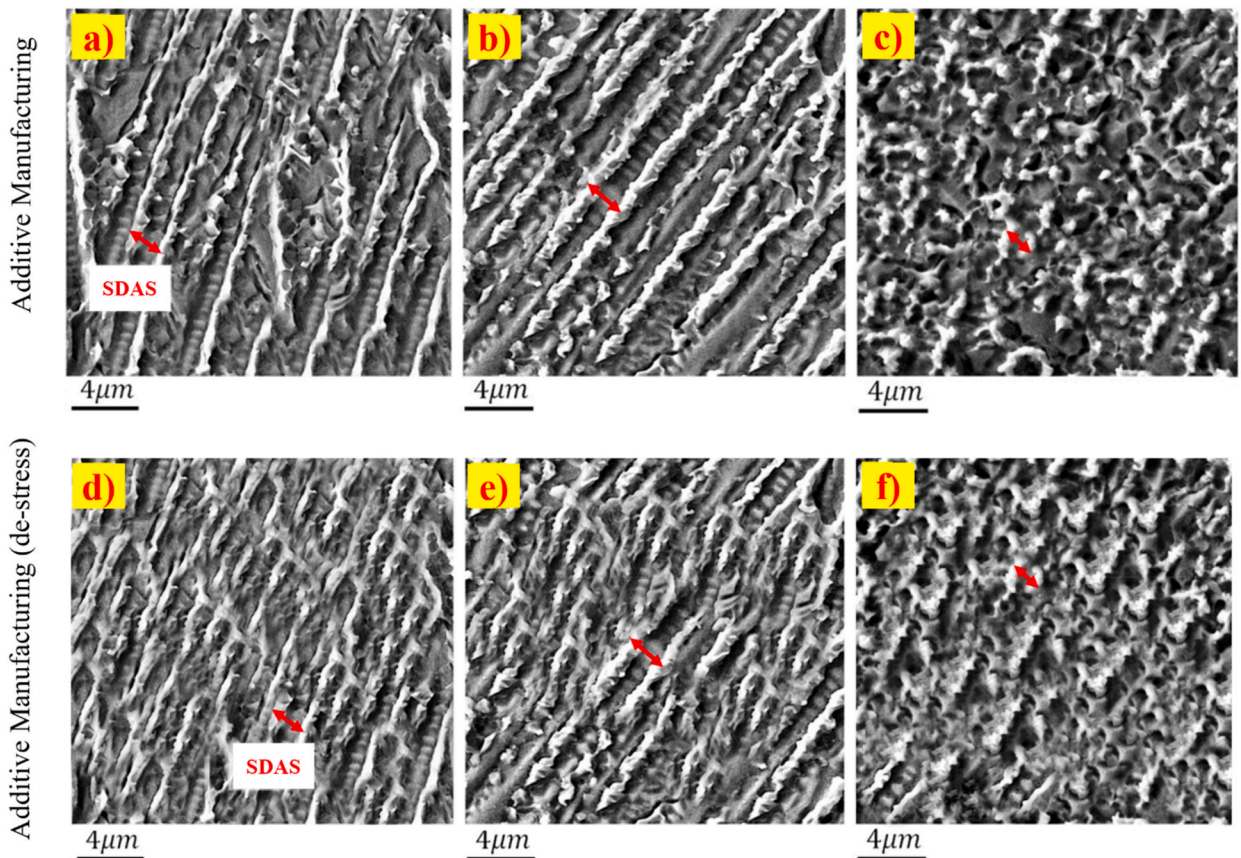**Fig. 2.** X-ray diffraction analysis results of a) substrate and b) DLD clad.

Fig. 3. a) Additive manufacturing sample, b)schematic of the tensile sample, and c) The top surface of the sample as-fabrication.

Fig. 4. Microstructure of secondary dendrite arm spacing in AM sample(a-e) and de-stressed sample (d–f): a,d) the zone of the interface between the clad and the substrate, b,e) middle zone of clad, and c,f) near the surface of clad.

perpendicular direction of the laser scanning. According to this Figure, both the substrate and the deposited cladding mainly contain FCC nickel-based austenitic phase (gamma phase). In both of them, peaks 111, 200, 220, 311, and 222 were identified in the diffraction pattern.

Fig. 3(a) and (b), and 3(c) show a schematic of the DLD process, the dimensions of the tensile sample used in this research and the top surface of the sample while being cladded. Tensile tests were performed according to ISO6892 standard and tensile rate 0.01 mm/s [24] by the Zwick Z250 machine (Repeat at least 2 times). Stress relief heat treatment for the sample was done at a temperature of 450 °C for 2 h [25–27].

To analyze the size of the structure manufactured via the direct laser deposition and to check the rate of cooling, the distance of the secondary dendrite arms was checked in three locations, i.e., interface, middle, and near the surface. The distance of the secondary arms of dendrites and the rate of cooling can be correlacted as Eq. (1) [28]:

$$\lambda_2 = A(G \times R)^{-n} \tag{1}$$

where λ_2 is the distance of the secondary dendrite arms, $G \times R$ (Thermal gradient and dendrite growth rate) is the cooling speed, while A and n are constants representing the materials. It can be observed that the distance of the dendritic arm has an inverse relationship with the rate of cooling and the temperature gradient. The laser deposition process is usually characterized with a very high temperature gradient ($\sim 10^6$ K/mm), therefore the obtained microstructure is expected to be fine-grained, and thus, λ will be reduced [29–33]. Also, A and n for laser-deposited Inconel 625 are equal to 34 and -0.33, respectively [28–33]. Electrochemical process of 1 gr chromic acid (CrO_3) and 10 ml distilled water (with a voltage of 10 V for 8 s) using a solution at 25 °C temperature. The process of calculating the rate of cooling in three regions, namely the interface, the middle region, and near the deposition surface, included the measurement of the distance between the secondary arms of the dendrite in each zone (with 20 repetitions), which was averaged for the calculation.

To evaluate the hardness of additive manufacturing parts before and after stress relaxation, the Vickers microhardness test with a load of 300 g was used [34]. Residual stress was done according to standards ASTM E915-2019 and ASTM E1426-2019 by the lateral slope method using the Proto LXRD system (Repeat at least 3 times). In this evaluation, the samples were separated from the substrate before measuring the residual stress. Mechanical polishing, followed by electrochemical polishing was performed to reveal the residual

Table 2
The average values of the distance between the secondary arms and the rate of cooling calculated in 3 zones (average of 15 measurements).

Structure	Cooling rate (G*R) (k/s)	Secondary Dendritic Arm Spacing (μm)	Zone in cladding
Columnar dendrite	$7.07 * 10^4$	3.90 ± 0.04 (μm)	near the interface
Columnar dendrite	$4.01 * 10^5$	2.21 ± 0.06 (μm)	middle zone (0.5 mm upper than the interface)
equiaxed dendrites	$1.07 * 10^6$	1.59 ± 0.04 (μm)	near the surface of the cladding (1.5 mm upper than the interface)
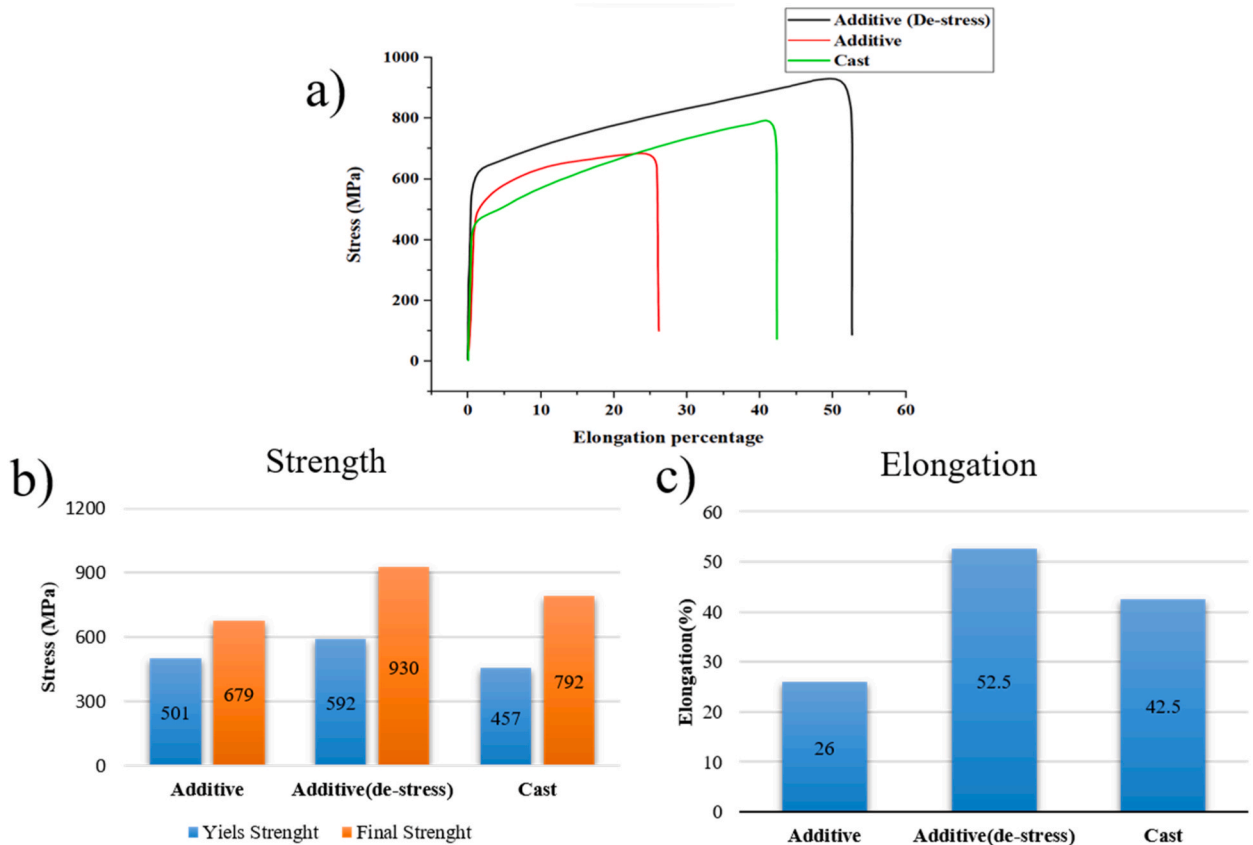
Fig. 5. a) Stress-strain diagram of additive manufacturing, stress relieved, and the substrate samples, b) Strength comparison of samples, and c) Elongation comparison of samples.

stress of the inner part [35–38]. In this research, for the residual stress of the samples, a peak with an angle of $2\theta = 92.5°$ and in the range of $2\theta = 88$-$93°$ was used. For all samples, the $(d$-$d_0)/d_0$ graph was drawn regarding $\sin^2\psi$. The residual stress test was performed for angles Psi $= -10°$, $-20°$, $-30°$, $0°$, $15°$, $30°$, and $45°$, and Eq. 2 was used to perform the calculations [39];

$$\sigma = \frac{m.E}{1 + \vartheta} \tag{2}$$

where m is the slope of the strain diagram regarding $\sin^2\psi$, E is Young's modulus, and ϑ is Poisson's ratio. An ultrasonic device equipped with a TR probe was used to measured Young's modulus and Poisson's ratio [40,41]. Then, using Eq. (3), Young's modulus equal to 175 ± 17 (average of 5 measurements) was obtained:

$$E = \rho * V^2 \tag{3}$$

3. Results and discussion

Fig. 4 depicts the solidification microstructure and SDAS in AM sample (Fig. 4(a–c)) and de-stressed sample (Fig. 4(d–f)) in the zone of the interface between the clad and the substrate, middle zone of clad, and near the surface of clad, respectively. The SDAS and Cooling rate are given in Table 2. According to this Table, the SDAS is reduced while traversing away from the interface. This stems
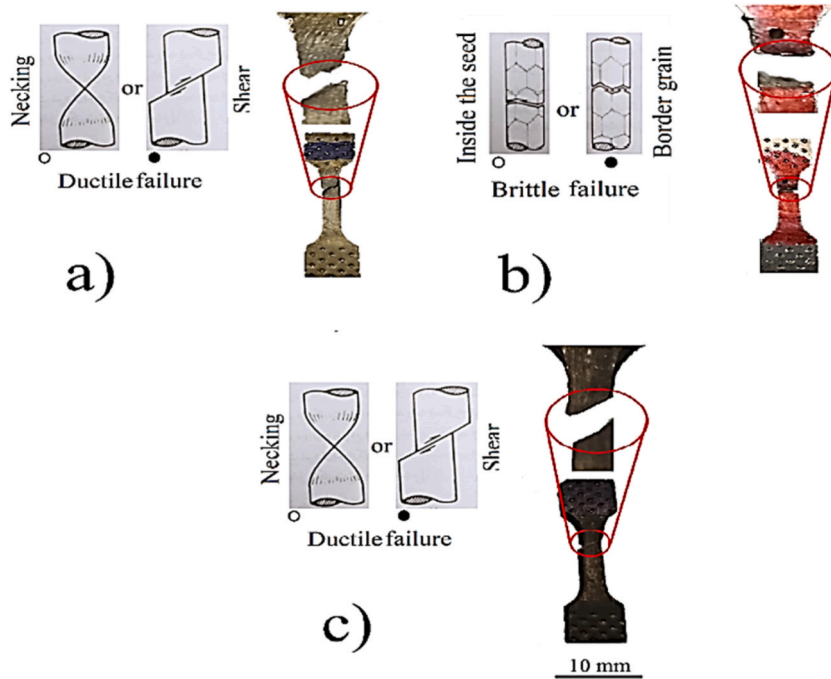
Fig. 6. Macro picture of the sample after failure a) cast sample, b) additive manufactured sample and c) additive manufactured sample (de-stress).

from the different rates of cooling at different points of the clad, so the cooling rate has increased from the interface ($7.07 * 10^4$ K /s) to the surface of the clad($1.07 * 10^6$ K /s). The structure of near the cladding surface is finer and the average distance between the dendritic arms from the interface to the surface is reduced. It is noteworthy that the distance between the arms of the secondary dendrite before and after de-stressing did not change significantly.

The stress-strain diagram for the substrate (casting sample) as a reference sample, the AM sample, and the sample after stress relaxation are represented in Fig. 5(a). As can be seen more clearly in Fig. 5(b) and 5(c), the yield strength of the AM sample is 506 MPa, representing a 10% increase in comparison with the reference sample. However, the final strength is reduced by 13%. In addition, the ductility significantly reduced from 42.5% to 26%. It is mainly due to the low heat transfer coefficient of Inconel 625 super alloy, 9.8 W/m.K, which is approximately one-sixteenth of aluminum and one-fortieth of copper [42,43]. Low heat transfer causes heat accumulation in the clad, and during the deposition of sequential layers in additive manufacturing process, it will lead to residual stress.

Fig. 6 shows the macro images of the sample's fracture surface. Fig. 6(a) demonstrates the cast sample where the shear-type ductile failure can be observed. This mechanism can be related to the crystallographic cross-slip of FCC crystal plates during fracture [44]. Fig. 6(b) shows the additive manufacturing sample, the brittle fracture that occurred in this case is a type of grain boundary fracture. It can be observed that the cross-sectional view of the fracture free of plastic deformation, considering that the metal in question has an FCC crystallographic structure and this type of fracture is not common in it. There was borderline brittleness. The temperature of the test is 25 °C and this case cannot be related to low temperature [45]. Fig. 6(c) shows the additive manufacturing sample (de-stressed). In this case, the ductile fracture occurs like the cast sample, and it seems that the grain boundary brittleness has been destroyed by the de-stressing process [45].

The SEM image represeting the surface of the fracture can be observed in Fig. 7. Fig. 7(a and b) and 7(e,f) are related to the casting sample and the additive manufacturing sample (de-stressed), respectively. Both structures show ductile fracture, and dimples are observed in two cases. Fig. 7(e–f) has more prominent dimple circles, which indicates more ductility in this case. Also, Fig. 7(c and d) shows the brittle fracture cross-section. The reason for the absence of a sharp and clear cleavage surface, in this case, is the type of failure, which was the grain boundary.

Residual stresses can cause defects such as cracks, reduction of strength or mechanical life, and dimensional inaccuracy due distortion in part. Regarding magnitude, the local residual stresses can contribute to a high percentage of the yield stress of the material (up to75%). Generally, additivly manufacturing parts are entangled with the significant residual stresses [1,2], which is influenced by process parameters including laser power, scanning velocity, overlap percentage and characteristics of the substrate and powder. By optimizing these parameters and features, the residual stress can be reduced to a great extent, but still, some amounts of residual stress remain in the workpiece [16–18,46,47]. Fig. 8 shows the strain diagram regarding $\sin^2\psi$ for the additive manufacturing sample. The fitted line of this graph follows the equation of y = 0.0031x - 0.0001. Using Eq. (2) and placing m = 0.0031, ϑ = 0.5, and Young's modulus equal to 175 GPa, the tensile residual stress equal to 361 MPa was obtained.

At low temperatures, when the tensile residual stress exceeds the tensile strength of the material, the possibility of cold cracking in
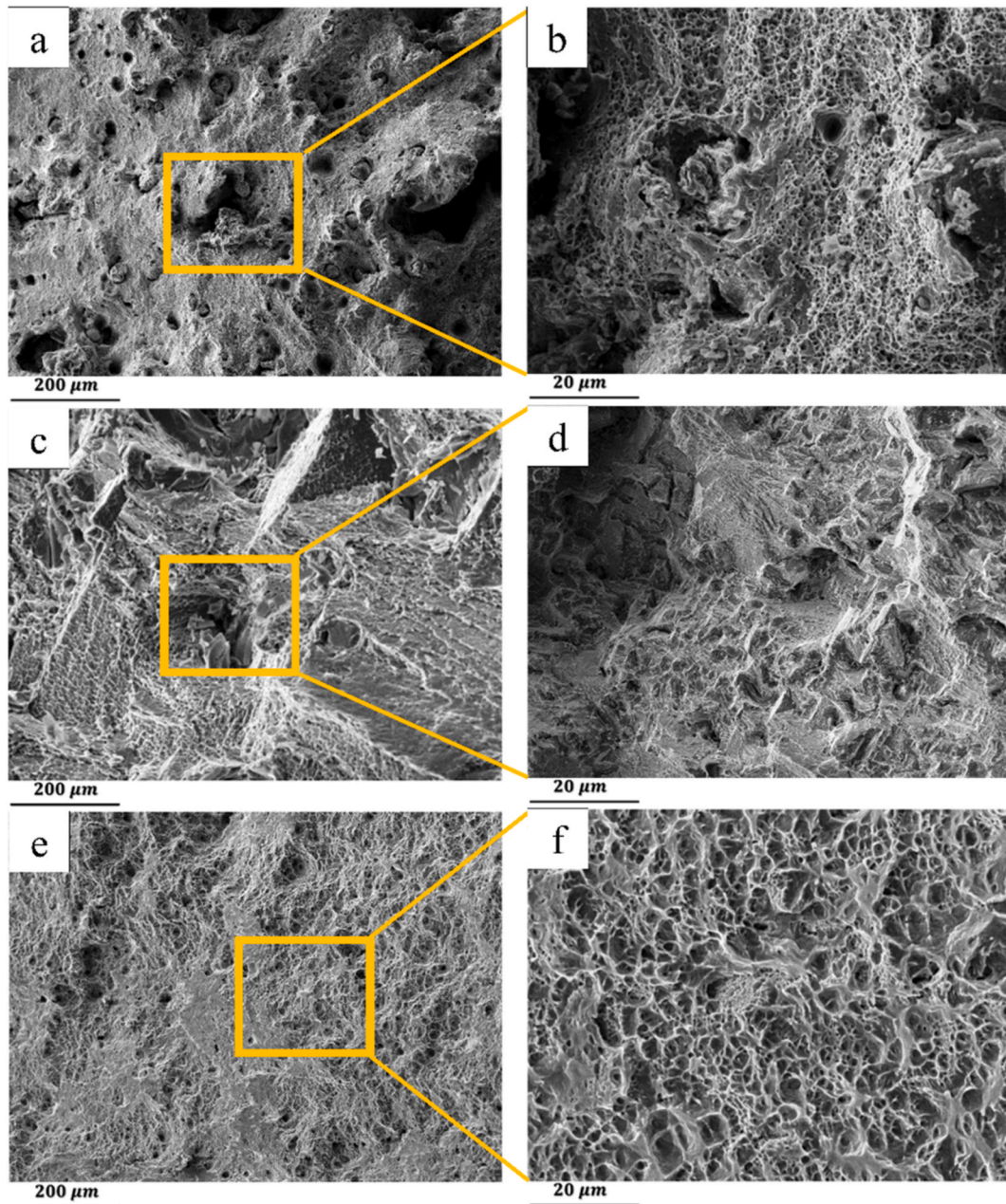
Fig. 7. SEM micrograph of fracture surface in (a,b) casting sample, (c,d) AM sample and (e,f) additive manufactured (de-stressed) sample.

the sample increases. Also, if the residual stress is high in the piece, a macroscopic crack is created. The formation of these cracks reduces the dimensional accuracy, ductility, and strength of the additively manufactured parts; Also, there are other mechanical properties which are impacted by residual stresses namely, corrosion resistance, fracture toughness, crack growth behavior, and fatigue performance [47]. Therefore, implementing preventative measures regarding crack nucleation in part by modifying the process and optimizing the parameters using methods such as stress relief operation, is of utmost importance [1,36,39].

Fig. 9 shows the strain diagram regarding $\sin^2\psi$ for the de-stress sample. The equation of the fitted line is y = 0.00024x + 0.00005. By setting m = 0.0002, ϑ = 0.5, and Young's modulus equal to175 GPa in Eq. (2), tensile residual stress equal to 23 MPa was obtained, which indicates almost complete relaxation of the residual stress.

According to Fig. 5, the yield strength increased from 506 MPa to 605 MPa by applying stress relieving heat treatment. Also, ductility increased from 26% to 52.5%. This amount of ductility is even higher than the reference(casting) sample. The remarkable point is the reduction of the residual stress from 361 to 23 MPa after the stress relaxation, equivalent to a change of 338 MPa, while the yield strength variation was equal to 99 MPa. It stems from the non-uniformity of residual stress distribution along each layer and the
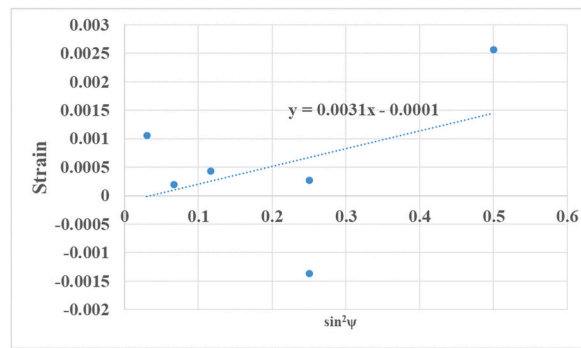
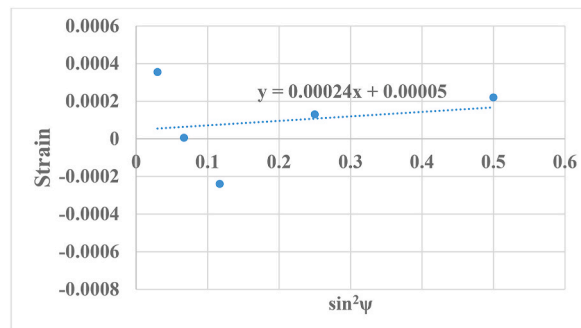**Fig. 8.** Strain-sin$^2\psi$ diagram after additive manufacturing.

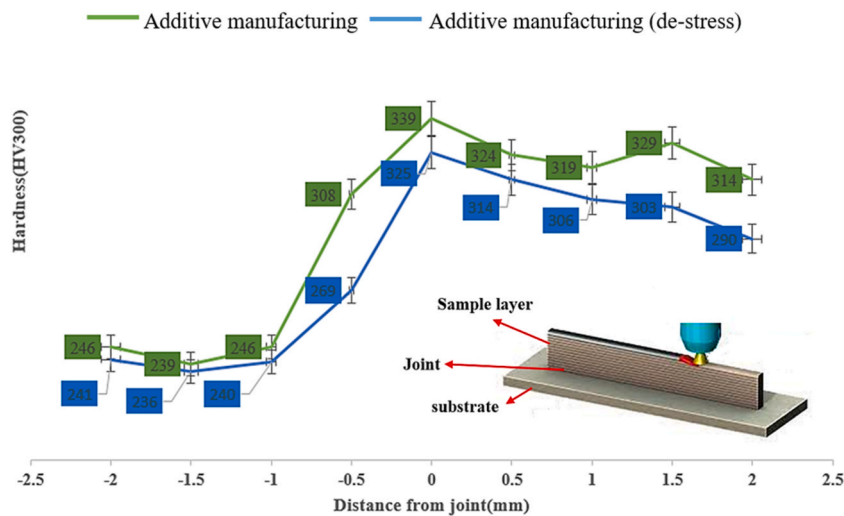**Fig. 9.** Strain-sin$^2\psi$ diagram of additive manufacturing sample (de-stress).

Fig. 10. Comparison of sample hardness changes based on the distance from the interface in the two cases of Additive manufacturing and additive manufacturing sample after stress release.

unbalanced distribution of residual stress in different layers, which has been mentioned in various studies [48–53].

The ultimate strength is reached from 679MPa in AM sample to 930 MPa in the de-stressed sample, which shows a 17% and 36% increase compared to the cast and AM samples, respectively.

Fig. 10 shows the hardness of the sample based on the distance from the interface. In this evaluation, the average hardness of five samples deposited layer is shown in two states before and after stress relaxation. Generally, in both cases, the hardness of the samples were reduced when moving from the interface zone to near the cladding surface. Generally, the solidified structure of parts resulting from laser additive manufacturing processes includes two competitive and cellular zones. During the deposition process, heat is

exchanged from the substrate, and therefore, the temperature flows perpendicular to the surface of the substrate. These zones are characterized with competitive growth where the oriented columnar dendrites are formed. In other zones, the growth is cellular. Still, at farther distances, the governing mechanism of solidification is determined according to the temperature gradient and the appropriate direction of crystallography in the metal [1,54,55]. In the stress-relieved sample, hardness has reduced slightly, but the significant point is the reduced fluctuations of the hardness at different issues due to the removal of residual stress throughout the workpiece, which leads to the improvement of the mechanical behavior of the workpiece.

4. Conclusion

This research was aimed to investigate the effect of residual stress in the additive manufacturing of Inconel 625 on the same substrate by the direct laser deposition process. The results showed.

1) Increasing cooling rate $7.07*10^4$ k/s to $1.07*10^7$ k/s and structure changes from columnar dendritic to coaxial dendritic,
2) 10% increase in the yield strength of the additively manufactured sample in the raw state compared to the cast sample and reducing its ductility from 42.5% to 26%, the presence of 361 MPa residual stress in the sample after additive manufacturing and reducing the tensile properties of the sample in this state,
3) almost complete elimination of residual stress which was the result of a 2 h heat treatment at 450 °C and significant improvement of ductility and strength compared to both casting (control) and additive manufacturing, Increase in ductility from 26% in additive manufacturing to 52.5% after stress relief and 17% and 36% increase in ultimate strength, respectively, compared to the cast sample and additive manufacturing sample, and decrease in fluctuations and hardness due to stress relief operation.

Author contribution statement

Mohammad Reza Borhani: Mohammad Rajabi: Reza Shoja Razavi: Roohollah Jamaati: Conceived and designed the experiments; Performed the experiments; Analyzed and interpreted the data; Contributed reagents, materials, analysis tools or data; Wrote the paper. Mohammad Rajabi: Reza Shoja Razavi: Roohollah Jamaati:Conceived and designed the experiments; Performed the experiments; Analyzed and interpreted the data; Contributed reagents, materials, analysis tools or data.

Data availability statement

The authors do not have permission to share data.

Declaration of competing interest

The authors declare that they have no known competing financial interests or personal relationships that could have appeared to influence the work reported in this paper.

References

[1] X. Cai, T. Liu, X. Yan, Z. Cheng, L. Pan, Z. Tian, L. Luo, Y. Su, Effect of process parameters on microstructures and properties of Al–42Si alloy fabricated by selective laser melting, Heliyon 8 (6) (2022 Jun 1), https://doi.org/10.1016/j.heliyon.2022.e09680.
[2] C. Zeng, Y. Jia, J. Xue, X. Liu, Q. Dong, Influence of the thermal-fluid behavior on the microstructure evolution during the process of selective laser melting of Ti6Al4V, Heliyon 8 (11) (2022 Nov 1), https://doi.org/10.1016/j.heliyon.2022.e11725.
[3] K.V. Wong, A. Hernandez, A review of additive manufacturing, Int. Sch. Res. Notices 2012 (2012), https://doi.org/10.5402/2012/208760.
[4] X. Liu, J. Fan, Y. Song, P. Zhang, F. Chen, R. Yuan, J. Wang, B. Tang, H. Kou, J. Li, High-temperature tensile and creep behaviour of Inconel 625 superalloy sheet and its associated deformation-failure micromechanisms, Mater. Sci. Eng., A 829 (2022 Jan 1), 142152, https://doi.org/10.1016/j.msea.2021.142152.
[5] V. Shankar, K.B. Rao, S.L. Mannan, Microstructure and mechanical properties of Inconel 625 superalloy, J. Nucl. Mater. 288 (2–3) (2001 Feb 1) 222–232, https://doi.org/10.1016/S0022-3115(00)00723-6.
[6] S.G. Chen, H.J. Gao, Q. Wu, Z.H. Gao, X. Zhou, Review on residual stresses in metal additive manufacturing: formation mechanisms, parameter dependencies, prediction and control approaches, J. Mater. Res. Technol. 17 (2022 Mar 1) 2950–2974, https://doi.org/10.1016/j.jmrt.2022.02.054.
[7] M. Rombouts, G. Maes, M. Mertens, W. Hendrix, Laser metal deposition of Inconel 625: microstructure and mechanical properties, J. Laser Appl. 24 (5) (2012 Nov 1), https://doi.org/10.2351/1.4757717.
[8] G.P. Dinda, A.K. Dasgupta, J. Mazumder, Laser aided direct metal deposition of Inconel 625 superalloy: microstructural evolution and thermal stability, Mater. Sci. Eng., A 509 (1–2) (2009 May 25) 98–104, https://doi.org/10.1016/j.msea.2009.01.009.
[9] F. Kermani, R. Shoja-Razavi, K. Zangenemadar, M. Borhani, M. Gavahian, An investigation into the effect of scanning pattern and heat treatment on the mechanical properties of Inconel 718 in the direct metal deposition process, J. Mater. Res. Technol. 24 (2023 May 1) 4743–4755, https://doi.org/10.1016/j.jmrt.2023.04.109.
[10] R. Li, G. Wang, X. Zhao, F. Dai, C. Huang, M. Zhang, X. Chen, H. Song, H. Zhang, Effect of path strategy on residual stress and distortion in laser and cold metal transfer hybrid additive manufacturing, Addit. Manuf. 46 (2021 Oct 1), 102203, https://doi.org/10.1016/j.addma.2021.102203.
[11] A. Serjouei, S. Afazov, Predictive model to design for high cycle fatigue of stainless steels produced by metal additive manufacturing, Heliyon 8 (11) (2022 Nov 1), https://doi.org/10.1016/j.heliyon.2022.e11473..
[12] C. Li, Z.Y. Liu, X.Y. Fang, Y.B. Guo, Residual stress in metal additive manufacturing, Procedia Cirp 71 (2018 Jan 1) 348–353, https://doi.org/10.1016/j.procir.2018.05.039.
[13] S. Kou, Welding metallurgy 431 (446) (2003 Sep) 223–225, https://doi.org/10.1557/mrs2003.197. New Jersey, USA.
[14] S. Jelvani, R. Shoja Razavi, M. Barekat, M. Dehnavi, Empirical-statistical modeling and prediction of geometric characteristics for laser-aided direct metal deposition of Inconel 718 superalloy, Met. Mater. Int. 26 (2020 May) 668–681, https://doi.org/10.1007/s12540-019-00355-7.

[15] X. Wang, C. Chen, L. Qin, M. Zhang, Microstructure evolution and mechanical behavior of inconel 625 produced using direct laser metal deposition, Phys. Met. Metallogr. 122 (2021 Sep) 896–907, https://doi.org/10.1134/S0031918X2109012X.

[16] P. Aggarangsi, J.L. Beuth, Localized preheating approaches for reducing residual stress in additive manufacturing, in: In2006 International Solid Freeform Fabrication Symposium, 2006, https://doi.org/10.26153/tsw/7174.

[17] M. Shiomi, K. Osakada, K. Nakamura, T. Yamashita, F. Abe, Residual stress within metallic model made by selective laser melting process, Cirp Annals 53 (1) (2004 Jan 1) 195–198, https://doi.org/10.1016/S0007-8506(07)60677-5.

[18] E.R. Denlinger, J.C. Heigel, P. Michaleris, T.A. Palmer, Effect of inter-layer dwell time on distortion and residual stress in additive manufacturing of titanium and nickel alloys, J. Mater. Process. Technol. 215 (2015 Jan 1) 123–131, https://doi.org/10.1016/j.jmatprotec.2014.07.030.

[19] M. Megahed, H.W. Mindt, N. N'Dri, H. Duan, O. Desmaison, Metal additive-manufacturing process and residual stress modeling, Integrating Materials and Manufacturing Innovation 5 (2016 Dec) 61–93, https://doi.org/10.1186/s40192-016-0047-2.

[20] V.V. Popov, A. Katz-Demyanetz, A. Koptyug, M. Bamberger, Selective electron beam melting of Al0. 5CrMoNbTa0. 5 high entropy alloys using elemental powder blend, Heliyon 5 (2) (2019 Feb 1), https://doi.org/10.1016/j.heliyon.2019.e01188.

[21] N. Grilli, D. Hu, D. Yushu, F. Chen, W. Yan, Crystal plasticity model of residual stress in additive manufacturing using the element elimination and reactivation method, Comput. Mech. (2021 Nov 26) 1–21, https://doi.org/10.1007/s00466-021-02116-z.

[22] M.R. Borhani, M. Rajabi, R. Shojarazavi, R. Jamaati, Statistical modeling in the laser cladding process of Inconel 625 via linear regression and response surface method, J. Laser Appl. 35 (2) (2023 May 1), https://doi.org/10.2351/7.0000964.

[23] R.S. Razavi, K. Zangenemadar, M. Borhani, M. Gavahian, Optimization of single-pass geometric characteristics of IN718 by fiber laser via linear regression and response surface method, J. Mater. Res. Technol. 24 (2023 May 1) 274–289, https://doi.org/10.1016/j.jmrt.2023.02.212.

[24] ISO 6892-1, Metallic Materials - Tensile Testing - Part 1: Method of Test at Room Temperature, 2019.

[25] Z. Tian, C. Zhang, D. Wang, W. Liu, X. Fang, D. Wellmann, Y. Zhao, Y. Tian, A review on laser powder bed fusion of inconel 625 nickel-based alloy, Appl. Sci. 10 (1) (2019 Dec 20) 81, https://doi.org/10.3390/app10010081.

[26] H. Liu, C.K. Tan, Y. Wei, S.H. Lim, C.J. Lee, Laser-cladding and interface evolutions of inconel 625 alloy on low alloy steel substrate upon heat and chemical treatments, Surf. Coating. Technol. 404 (2020 Dec 25), 126607, https://doi.org/10.1016/j.surfcoat.2020.126607.

[27] Ams5662, Standard for Nickel Alloy, Corrosion and Heat-Resistant, Bars, Forgings, and Rings 52.5Ni - 19Cr - 3.0Mo - 5.1Cb (Nb) - 0.90Ti - 0.50Al - 18Fe Consumable Electrode or Vacuum Induction Melted 1775 °F (968 °C) Solution Heat Treated, Precipitation-Hardenable, 2016.

[28] G. Meng, Y. Gong, J. Zhang, L. Zhu, H. Xie, J. Zhao, Multi-scale simulation of microstructure evolution during direct laser deposition of Inconel718, Int. J. Heat Mass Tran. 191 (2022 Aug 1), 122798, https://doi.org/10.1016/j.ijheatmasstransfer.2022.122798.

[29] S. Jelvani, R.S. Razavi, M. Barekat, M.R. Dehnavi, M. Erfanmanesh, Evaluation of solidification and microstructure in laser cladding Inconel 718 superalloy, Opt Laser. Technol. 120 (2019 Dec 1), 105761, https://doi.org/10.1016/j.optlastec.2019.105761.

[30] A.A. Ferreira, O. Emadinia, R.L. Amaral, J.M. Cruz, A.R. Reis, M.F. Vieira, Mechanical and microstructural characterisation of Inconel 625-AISI 431 steel bulk produced by direct laser deposition, J. Mater. Process. Technol. 306 (2022 Aug 1), 117603, https://doi.org/10.1016/j.jmatprotec.2022.117603.

[31] K.O. Yu (Ed.), Modeling for Casting and Solidification Processing, CRC Press, 2001 Oct 16.

[32] M. Hong, S. Wang, W. Sun, Z. Geng, J. Xin, L. Ke, Effect of welding speed on microstructure and mechanical properties of selective laser melting Inconel 625 alloy laser welded joint, J. Mater. Res. Technol. 19 (2022 Jul 1) 2093–2103, https://doi.org/10.1016/j.jmrt.2022.06.020.

[33] M. Ahmad, G. Ali, E. Ahmed, M.A. Haq, J.I. Akhter, Novel microstructural growth in the surface of Inconel 625 by the addition of SiC under electron beam melting, Appl. Surf. Sci. 257 (17) (2011 Jun 15) 7405–7410, https://doi.org/10.1016/j.apsusc.2011.02.067.

[34] ASTM E384 -17, Standard Test Method, for Microindentation Hardness of Materials, 2018.

[35] G.U. Jiang, F.U. Haiyang, P.A. Bo, K.A. Renke, Recent progress of residual stress measurement methods: a review, Chin. J. Aeronaut. 34 (2) (2021 Feb 1) 54–78, https://doi.org/10.1016/j.cja.2019.10.010.

[36] J.L. Bartlett, X. Li, An overview of residual stresses in metal powder bed fusion, Addit. Manuf. 27 (2019 May 1) 131–149, https://doi.org/10.1016/j.addma.2019.02.020.

[37] W. Chen, T. Voisin, Y. Zhang, J.B. Forien, C.M. Spadaccini, D.L. McDowell, T. Zhu, Y.M. Wang, Microscale residual stresses in additively manufactured stainless steel, Nat. Commun. 10 (1) (2019 Sep 25) 4338, https://doi.org/10.1038/s41467-019-12265-8.

[38] P.J. Withers, Residual stress and its role in failure, Rep. Prog. Phys. 70 (12) (2007 Nov 27) 2211, https://doi.org/10.1088/0034-4885/70/12/R04.

[39] Fitzpatrick ME, Fry AT, Holdway P, Kandil FA, Shackleton J, Suominen L. Determination of residual stresses by X-ray diffraction, http://eprintspublications.npl.co.uk/id/eprint/2391.

[40] X. Qian, T. Ma, C.C. Shih, M. Heur, J. Zhang, K.K. Shung, R. Varma, M.S. Humayun, Q. Zhou, Ultrasonic microelastography to assess biomechanical properties of the cornea, IEEE (Inst. Electr. Electron. Eng.) Trans. Biomed. Eng. 66 (3) (2018 Jul 5) 647–655, https://doi.org/10.1109/TBME.2018.2853571.

[41] J. Carrillo, J. Ramirez, J. Lizarazo-Marriaga, Modulus of elasticity and Poisson's ratio of fiber-reinforced concrete in Colombia from ultrasonic pulse velocities, J. Build. Eng. 23 (2019 May 1) 18–26, https://doi.org/10.1016/j.jobe.2019.01.016.

[42] A. Magana, J. Yoshioka, M. Eshraghi, P. Allu, Multiphysics modeling of thermal behavior, melt pool geometry, and surface topology during laser additive manufacturing, Mater. Des. 219 (2022 Jul 1), 110831, https://doi.org/10.1016/j.matdes.2022.110831.

[43] L.C. Wei, L.E. Ehrlich, M.J. Powell-Palm, C. Montgomery, J. Beuth, J.A. Malen, Thermal conductivity of metal powders for powder bed additive manufacturing, Addit. Manuf. 21 (2018 May 1) 201–208, https://doi.org/10.1016/j.addma.2018.02.002.

[44] C.R. Brooks, A. Choudhury, Failure Analysis of Engineering Materials, McGraw-Hill Education, 2002.

[45] D. Hull, Fractography: Observing, Measuring and Interpreting Fracture Surface Topography, Cambridge University Press, 1999 Sep 23.

[46] J. Song, L. Zhang, W. Wu, B. He, X. Ni, J. Xu, G. Zhu, Q. Yang, T. Wang, L. Lu, Understanding processing parameters affecting residual stress in selective laser melting of Inconel 718 through numerical modeling, J. Mater. Res. 34 (8) (2019 Apr) 1395–1404, https://doi.org/10.1557/jmr.2018.504.

[47] P. Hanzl, M. Zetek, T. Bakša, T. Kroupa, The influence of processing parameters on the mechanical properties of SLM parts, Procedia Eng. 100 (2015 Jan 1) 1405–1413, https://doi.org/10.1016/j.proeng.2015.01.510.

[48] T. Mukherjee, W. Zhang, T. DebRoy, An improved prediction of residual stresses and distortion in additive manufacturing, Comput. Mater. Sci. 126 (2017 Jan 1) 360–372, https://doi.org/10.1016/j.commatsci.2016.10.003.

[49] M. Mansouri, A. Kazerooni, M.M. Fallah, Experimental study of residual stress in parts with variable cross section in selective laser melting process, Iran. J. Manuf. Eng. 9 (2) (2022 Apr 21) 8–17, https://doi.org/10.22034/ijme.2022.157558.

[50] E. Mirkoohi, J.R. Dobbs, S.Y. Liang, Analytical modeling of residual stress in direct metal deposition considering scan strategy, Int. J. Adv. Des. Manuf. Technol. 106 (2020 Feb) 4105–4121, https://doi.org/10.1007/s00170-019-04919-0.

[51] F. Hajializadeh, A. Ince, Integration of artificial neural network with finite element analysis for residual stress prediction of direct metal deposition process, Mater. Today Commun. 27 (2021 Jun 1), 102197, https://doi.org/10.1016/j.mtcomm.2021.102197.

[52] N.W. Klingbeil, J.L. Beuth, R.K. Chin, C.H. Amon, Residual stress-induced warping in direct metal solid freeform fabrication, Int. J. Mech. Sci. 44 (1) (2002 Jan 1) 57–77, https://doi.org/10.1016/S0020-7403(01)00084-4.

[53] X. Zhao, A. Iyer, P. Promoppatum, S.C. Yao, Numerical modeling of the thermal behavior and residual stress in the direct metal laser sintering process of titanium alloy products, Addit. Manuf. 14 (2017 Mar 1) 126–136, https://doi.org/10.1016/j.addma.2016.10.005.

[54] L. Costa, R. Vilar, Laser powder deposition, Rapid Prototyp. J. 15 (4) (2009 Jul 31) 264–279, https://doi.org/10.1108/13552540910979785.

[55] M. Rashkovets, A. Nikulina, G. Turichin, O. Klimova-Korsmik, M. Sklyar, Microstructure and phase composition of Ni-based alloy obtained by high-speed direct laser deposition, J. Mater. Eng. Perform. 27 (2018 Dec) 6398–6406, https://doi.org/10.1007/s11665-018-3722-y.